AFRL-PR-WP-TP-2006-261

PERFORMANCE OF PYLONS UPSTREAM OF A CAVITY-BASED FLAMEHOLDER IN NON-REACTING SUPERSONIC FLOW (POSTPRINT)

Lane C. Haubelt, Paul I. King, Mark R. Gruber, Campbell D. Carter, and Kuang-Yu (Mark) Hsu

OCTOBER 2006

STINFO COPY

PROPULSION DIRECTORATE
AIR FORCE MATERIEL COMMAND
AIR FORCE RESEARCH LABORATORY
WRIGHT-PATTERSON AIR FORCE BASE, OH 45433-7251

REPORT DOCUMENTATION PAGE

The public reporting burden for this collection of information is estimated to average 1 hour per response, including the time for reviewing instructions, searching existing data sources, searching existing data sources, gathering and maintaining the data needed, and completing and reviewing the collection of information. Send comments regarding this burden estimate or any other aspect of this collection of information, including suggestions for reducing this burden, to Department of Defense, Washington Headquarters Services, Directorate for Information Operations and Reports (0704-0188), 1215 Jefferson Davis Highway, Suite 1204, Arlington, VA 22202-4302. Respondents should be aware that notwithstanding any other provision of law, no person shall be subject to any penalty for failing to comply with a collection of information if it does not display a currently valid OMB control number. **PLEASE DO NOT RETURN YOUR FORM TO THE ABOVE ADDRESS**.

1. REPORT DATE *(DD-MM-YY)*	2. REPORT TYPE	3. DATES COVERED *(From - To)*
October 2006	Conference Paper Postprint	N/A

4. TITLE AND SUBTITLE

PERFORMANCE OF PYLONS UPSTREAM OF A CAVITY-BASED FLAMEHOLDER IN NON-REACTING SUPERSONIC FLOW (POSTPRINT)

5a. CONTRACT NUMBER
In-house

5b. GRANT NUMBER

5c. PROGRAM ELEMENT NUMBER
61102F

6. AUTHOR(S)

Lane C. Haubelt and Paul I. King (Air Force Institute of Technology)
Mark R. Gruber and Campbell D. Carter (AFRL/PRAS)
Kuang–Yu (Mark) Hsu (Innovative Scientific Solutions, Inc.)

5d. PROJECT NUMBER
2308

5e. TASK NUMBER
AI

5f. WORK UNIT NUMBER
00

7. PERFORMING ORGANIZATION NAME(S) AND ADDRESS(ES)

Air Force Institute of Technology
WPAFB, OH 45433

Propulsion Sciences Branch (AFRL/PRAS)
Aerospace Propulsion Division
Propulsion Directorate
Air Force Research Laboratory
Air Force Materiel Command
Wright-Patterson AFB, OH 45433-7251

Innovative Scientific Solutions, Inc.
Dayton, OH 45440

8. PERFORMING ORGANIZATION REPORT NUMBER

AFRL-PR-WP-TP-2006-261

9. SPONSORING/MONITORING AGENCY NAME(S) AND ADDRESS(ES)

Propulsion Directorate
Air Force Research Laboratory
Air Force Materiel Command
Wright-Patterson AFB, OH 45433-7251

10. SPONSORING/MONITORING AGENCY ACRONYM(S)
AFRL-PR-WP

11. SPONSORING/MONITORING AGENCY REPORT NUMBER(S)
AFRL-PR-WP-TP-2006-261

12. DISTRIBUTION/AVAILABILITY STATEMENT
Approved for public release; distribution is unlimited.

13. SUPPLEMENTARY NOTES
Conference paper postprint published in the Proceedings of the 2006 42nd AIAA/ASME/SAE/ASEE Joint Propulsion Conference and Exhibit.

© 2006 American Institute of Aeronautics and Astronautics, Inc. The U.S. Government is joint author of the work and has the right to use, modify, reproduce, release, perform, display, or disclose the work.

PAO case number: AFRL/WS 06-1233; Date cleared: 04 May 2006. Paper contains color.

14. ABSTRACT
Cavity-based fuel injection and flame holding, typically found in hydrocarbon-fueled scramjet applications, are of current interest for use in supersonic combustors. Both the Air Force Research Lab (AFRL) and the Air Force Institute of Technology (AFIT) at Wright-Patterson Air Force Base in Ohio are investigating the enhancement of fuel-air mixing with small pylons that project into the supersonic flow upstream of a flame holder cavity. The pylons were of three sizes (medium, tall, and wide) and shaped as a thin triangular wedge with a 300 inclination angle. A total of four configurations (pylons plus baseline) were tested at two different fuel injection pressures in a Mach continuous flow wind tunnel housed at AFRL. The goal was to measure the mixing efficiency and shock loss of each pylon setup for comparison to the baseline condition of transverse injection without pylons. Non-reacting flow was measured using intrusive and non intrusive techniques to obtain pitot pressure, total temperature, cone-static pressure and laser induced Raman spectroscopy to determine species concentration over the cavity.

15. SUBJECT TERMS

16. SECURITY CLASSIFICATION OF:			17. LIMITATION OF ABSTRACT:	18. NUMBER OF PAGES	19a. NAME OF RESPONSIBLE PERSON (Monitor)
a. REPORT Unclassified	**b. ABSTRACT** Unclassified	**c. THIS PAGE** Unclassified	SAR	26	Campbell D. Carter
					19b. TELEPHONE NUMBER *(Include Area Code)* N/A

Standard Form 298 (Rev. 8-98)
Prescribed by ANSI Std. Z39-18

i

Performance of Pylons Upstream of a Cavity-based Flameholder in Non-reacting Supersonic Flow

Lane C. Haubelt[*] and Paul I. King,[†]
Air Force Institute of Technology, Wright-Patterson Air Force Base, OH 45433

Mark R. Gruber[‡] and Campbell D. Carter,[§]
Air Force Research Laboratory (AFRL/PRAS), Wright-Patterson Air Force Base, OH 45433

and

Kuang-Yu (Mark) Hsu[**]
Innovative Scientific Solutions, Inc., Dayton, OH, 45440

    Cavity-based fuel injection and flame holding, typically found in hydrocarbon-fueled scramjet applications, are of current interest for use in supersonic combustors. Both the Air Force Research Lab (AFRL) and the Air Force Institute of Technology (AFIT) at Wright-Patterson Air Force Base in Ohio are investigating the enhancement of fuel-air mixing with small pylons that project into the supersonic flow upstream of a flame holder cavity. The pylons were of three sizes (medium, tall, and wide) and shaped as a thin triangular wedge with a 30° inclination angle. A total of four configurations (pylons plus baseline) were tested at two different fuel injection pressures in a Mach continuous flow wind tunnel housed at AFRL. The goal was to measure the mixing efficiency and shock loss of each pylon setup for comparison to the baseline condition of transverse injection without pylons. Non-reacting flow was measured using intrusive and non intrusive techniques to obtain pitot pressure, total temperature, cone-static pressure and laser induced Raman spectroscopy to determine species concentration over the cavity downstream of the injection port. Results demonstrated that pylons increase fuel penetration, while not adding significantly to shock losses or overall mixing compared to baseline.

Nomenclature

A_f	=	flammable plume area
A_p	=	plume area
D	=	cavity depth
d	=	injection port diameter
h	=	pylon height
h_c/d	=	penetration of plume core
h_p/d	=	penetration of plume
L	=	cavity length
l	=	pylon length
M	=	Mach number
$\mathcal{M}$	=	molecule
n	=	power law rate variable

---

[*] Developmental Engineer, 412th TW/ENFB, Edwards AFB, CA, Non-Member
[†] Professor, Department of Aeronautics and Astronautics, AFIT/ENY, AIAA Senior Member
[‡] Senior Aerospace Engineer, AIAA Associate Fellow
[§] Senior Aerospace Engineer, AIAA Associate Fellow
[**] Senior Research Scientist, AIAA Senior Member

P_t	=	total pressure
$\bar{q}$	=	jet-to-freestream momentum flux ratio
u	=	freestream velocity
W	=	pylon width
X_i	=	mole fraction
X_p	=	spanwise centerline of injection port
x_{flam}	=	flammable mixture distance
x_{fm}	=	fully mixed distance
β	=	power law coefficient
Φ	=	equivalence ratio
Φ_{max}	=	maximum equivalence ratio
θ	=	pylon wedge angle
ρ	=	density
$\bar{\omega}$	=	total pressure loss coefficient

I.   Introduction

EFFICIENT fuel injection and mixing is critical to the successful development of a hypersonic air-breathing propulsion system. Supersonic velocities within the combustor section limit the time fuel can mix with the air flow. Surface interactions with the flow create undesirable losses and drag. A current area of interest is cavity-based flame holders within the combustor section. This type of flame holder has demonstrated lower drag than conventional intrusive designs, while providing a low momentum region for flame stabilization. [1,2] However, the need still remains for efficient methods of fuel injection.

Ongoing experimentation at the Air Force Research Laboratory Propulsion Directorate (AFRL/PR) at Wright-Patterson Air Force Base (WPAFB) aims to enhance supersonic combustion through pylon-aided transverse fuel injection. Intrusive devices such as pylons create disturbances in the flow which may be beneficial to fuel mixing and penetration. Thin, swept pylon geometries are employed to reduce aerodynamic losses while maintaining high mixing potential. [3]

Initial research utilizing pylons placed upstream of injection ports showed increased fuel penetration and the possibility for similar total pressure loss compared with transverse injection alone. Penetration lifts the fuel plume into the freestream and away from the combustor wall, shortening combustor length and preventing boundary layer flashback, or the ignition of fuel which has become entrained in the boundary layer. [4] Use of pylon injection systems may improve total combustor performance when coupled with cavity-based flame holders.

Previous work by Montes et al. [5] employed three pylons, configured with circular transverse injection ports at their base and installed upstream of a cavity flame holder employed at the AFRL Supersonic Combustion Facility. State-of-the-art non-intrusive visualization techniques were used to gather qualitative information regarding the ability of the pylons to improve fuel mixing and penetration at various injection pressures. The research was performed in a non-reacting Mach 2 flow environment. Each pylon was a triangular wedge with a 30° inclination. Pylon designs were based on the two best geometries determined from a computational study, [6] and correlated with sizes used in separate experimental work. [7,8] The research showed that pylons improved penetration and mixing potential over a baseline transverse injection case without a pylon. However, due to the techniques used, information on aerodynamic losses could not be obtained.

The purpose of the present research is to obtain quantitative data for pylon-aided injection upstream of a cavity flame holder. Using the three pylon configurations implemented in previous research at the Supersonic Combustion Facility, this experiment seeks to gain understanding in two areas: the pylons' effect on fuel mixing and supersonic aerodynamic losses.

II.   Methodology

## A. Test Facility and Hardware

The facility used is the Supersonic Combustion Facility of the Air Force Research Laboratory, Propulsion Directorate (AFRL/PR). The wind tunnel is designed to allow basic studies of principles governing supersonic

mixing and combustion processes using conventional and non-intrusive diagnostic techniques. A continuous supply of clean, compressed air is available to provide stagnation conditions up to 1660°R and 400 psia and a total maximum flow rate of 34 lbm/s. The wind tunnel is made up of five major components: the inlet, settling chamber, nozzle, test section and diffuser. Facility details are given by its chief designers, Gruber and Nejad.[9]

Several nozzles are available to provide Mach numbers from 2 to 4.5. The nozzle used for this experiment expands the flow to a Mach number of 2.0 at the test section entrance. Prior to the test section, a constant area isolator 7 inches in length begins immediately after the nozzle's 2 inch high by 6 inch wide exit. The isolator is followed by a 30 inch divergent floor ramp with a 2.5° slope. The entire test section is completely visible through fused silica windows, with excellent material properties for transmission of ultraviolet wavelengths used in common non-intrusive diagnostics (such as Raman scattering). Two windows mounted on either side wall enables full viewing of the transverse direction. Approximately 3 inches of spanwise viewing is available through a single window mounted on the top wall.

A modular cavity is mounted flush within the first 12 inches of the divergent test section floor. The cavity design accommodates various injection and combustion schemes. The cavity spans the entire width of the tunnel test section, and is recessed from the surface by a 90° backward-facing step to a depth (D) of 0.65 inches followed by a 22.5° trailing edge ramp. The total cavity length (L) is 2.6 inches producing an aspect ratio (L/D) of 4.0.

Four injection schemes, one baseline and three pylon, are used and placed approximately 0.35 inches upstream of the cavity's leading edge. The baseline scheme is a simple circular transverse injection port with a 0.062-in diameter. The three pylon schemes, termed medium, tall and wide, incorporate a thin intrusion just upstream of the transverse injection port and are of various sizes. The pylons' optimal heights, widths and distances from the injection port are determined from previous computational methods[6] and correlated to sizes used in prior experimentation.[7,8] Designs are determined from the top two configurations which show enhancement of fuel penetration. A schematic of the pylon and injector port design used in this research is given in Figure 1 below. Notice that the streamwise (x), transverse (y) and spanwise (z) coordinates are given in the figure, with origin at the center of the injection port at the surface. The pylon geometry is characterized by the length (l), height (h), width (W). The wedge angle (θ) is derived from l and h. As noted above, the injection port diameter, d, is constant at 0.062-in. The axial distance between the pylon's trailing edge and the port's spanwise centerline, X_p, is defined as the *injection proximity*. Pylon geometries are tabulated in Table 1. A profile schematic of the test assembly with a pylon insert is shown in Figure 2.
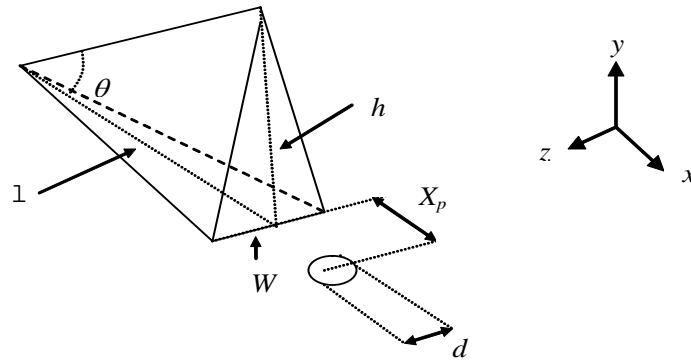
Figure 1. Pylon and injection port geometry[5]

American Institute of Aeronautics and Astronautics

Table 1. Geometries for the medium, tall and wide pylons[5]

		Medium	Tall	Wide
Height, _h_	**(in)**	0.25	0.375	0.25
Length, _l_	**(in)**	0.43	0.65	0.43
Width, _W_	**(in)**	0.07	0.07	0.1
Proximity, X_p	**(in)**	0.14	0.14	0.2
Wedge Angle, θ	**(deg)**	30.2	30	30.2
_h/d_	**(-)**	4	6	4
_W/d_	**(-)**	1.12	1.12	1.6
X_p/d	**(-)**	2.24	2.24	3.2
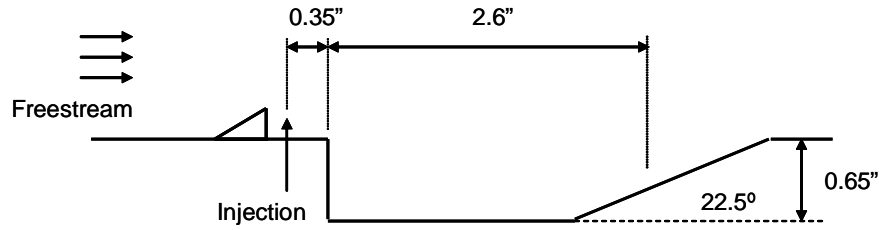
Figure 2. Pylon-cavity schematic

B. Testing Strategy

Tests are conducted with a main flow Mach number of 2.0. Freestream conditions are set for a total pressure of 50 psia and an average total temperature of 550º R. These values produce a freestream Reynolds number of 7.70 × 10^6 per foot, indicating a turbulent boundary layer at the injection station. Table 2 summarizes the freestream conditions at the nozzle exit. Gaseous ethylene (C_2H_4) is used as the injectant in all testing. The two separate injection pressures of 50 and 200 psia allow for a fuel mass flow rate of 3.5×10^{-3} and 1.4×10^{-2} lb/sec respectively.

Four measurements are used to interrogate the supersonic flow field: species sampling, pitot pressure, cone-static pressure and total temperature. Species composition sampling is performed using the non-intrusive Raman spectroscopy technique and allows for information into the jet mixing characteristics and fuel dispersion. The three remaining measurements are done using traditional aerothermodynamic probes and are used to determine total pressure and momentum losses. Finally, shadowgraph profile images are taken of the region of interest to allow orientation and illustration of the flow's physical features.

Measurements for all eight configurations (four schemes at two injection pressures) are performed 0.75 inches downstream of the injection port; this position is located above the spark plug in the flame holding cavity.

Table 2. Freestream conditions at nozzle exit

M_∞	2.0
$P_{t,\infty}$ _(psia)_	50
$T_{t,\infty}$ _(ºR)_	550
P_∞ _(psia)_	6.39
T_∞ _(ºR)_	306
a_∞ _(ft/sec)_	857
U_∞ _(ft/sec)_	1714
ρ_∞ _(lbm/ft³)_	0.056
γ_∞	1.4
$\dot{m}_\infty$ _(lbm/sec)_	8.0

American Institute of Aeronautics and Astronautics

Previous research indicates that the wide pylon shows the greatest potential for sustaining mixing while reducing total pressure and momentum losses when compared to the baseline configuration. Species sampling is performed at two additional axial locations over the cavity (0.45 and 1.85 inches) to determine mixing rates and trends for the wide and baseline configurations. Measurements are made in the transverse and spanwise coordinates using a two-dimensional data mesh. The size of the data mesh ($-0.5 \leq z \leq 0.5$ and $-0.25 \leq y \leq 1.0$) allows the ethylene fuel plume to be captured.

C. Species Composition Sampling

Species composition measurements are used to describe mixing in a supersonic flow with foreign gas injection. It is known that flow parameters such as Mach number and total pressure in a mixed gas environment are functions of the ratio of specific heats (γ).[10] For a gas of single species, calculation of the specific heats is based upon the conditions of the medium. However, for a mixture of gases, such as air and ethylene, each species have different specific heats. The following equation must be used to determine the specific heats of a mixture:

$$c_{p,mixture} = \sum X_i * c_{p,i} \qquad (1)$$

and

$$c_{v,mixture} = \sum X_i * c_{v,i} \qquad (2)$$

where X_i is the *mole fraction* of species *i*. Additionally, mixing analysis requires knowledge of local species concentration which can only be done through species composition sampling.

Species composition sampling is performed using a non-intrusive laser induced spontaneous Raman spectroscopy method. Raman spectroscopy takes advantage of the Raman scattering phenomenon that occurs when photons of light interact with individual molecules. Raman scattering can be considered an instantaneous (occurring within a time of 10^{-12} seconds or less) inelastic collision of an incident photon, ($\hbar_i$) with a molecule ($\mathcal{M}$) both at different discrete energy levels.[11] An inelastic process occurs when there is an exchange of energy occurring between $\hbar_i$ and M, emitting scattered light shifted from its original frequency.[12] For the method used in this experiment, the frequency of the scattered light is related to the vibrational frequency of the molecule. This scattered light from the medium is collected. The intensity of the collected light may be differentiated by frequency and related to the number densities of the species in the medium.

A schematic of the Raman spectroscopy setup used in the experiment is shown in Figure 3. The excitation source is provided by Spectra-Physics® Millenia Pro continuous wave (CW) laser producing 8.5 Watts at 532 nm. The scattered light is separated by frequency using a Kaiser Holospec™ f/1.8 imaging spectrometer and detected using an Andor® back-illuminated, thermo-electrically cooled spectroscopy CCD camera. The entire setup is placed on a two-axis traversing table with freedom of movement in the transverse and streamwise directions (tunnel *x* and *y*).
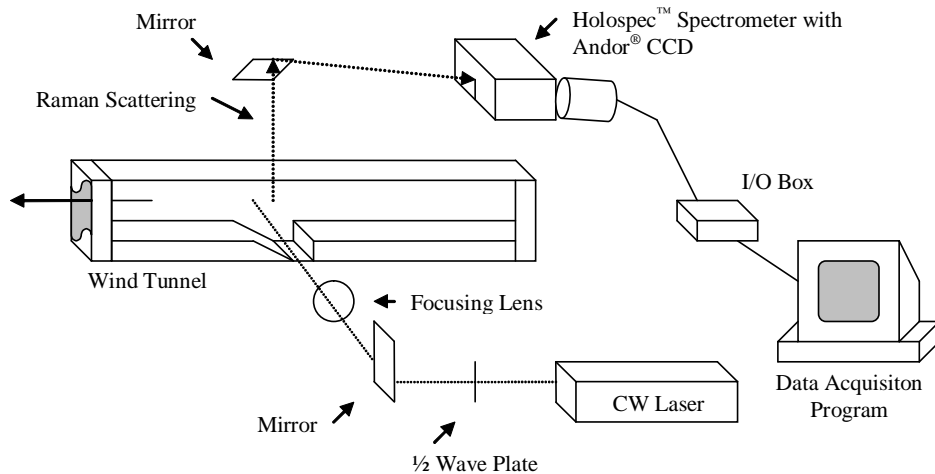
Figure 3. Schematic of planar Raman scattering setup used in experiment

D. Aerothermodynamic Probing

Three sets of conventional probes are used to examine the flow field at an axial location of 0.75 inches. Measurements are performed using a pitot, cone-static probe and total temperature probe with similar test meshes. All probes are approximately the same length with similar circular capture areas of 3.9×10^{-3} in^2 and are secured within identical 7.75 inch long and 1.0 inch wide diamond-wedge struts. Views of a typical probe setup are shown in Figure 4; the probe shown in the picture is the cone static (flow direction is indicated).
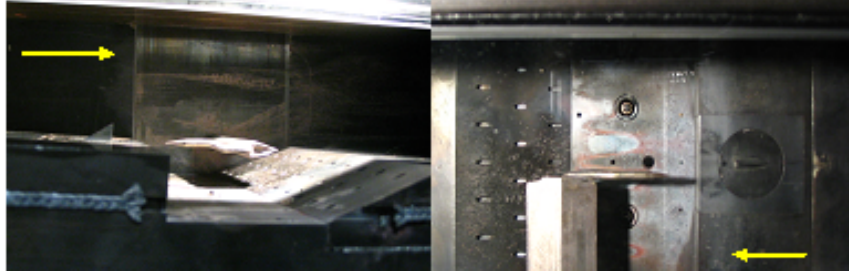

Figure 4. Cone-static probe installed in the tunnel

E. Data Reduction and Uncertainty

Using the ethylene concentration data, along with the pitot pressure, cone-static pressure and total temperature, the conditions such as total pressure and Mach number can be determined at the probing axial location ($x = 0.75$ in). Since very little is known of the actual properties, an iterative solution is necessary. A computerized solution algorithm developed by Fuller[13] uses compressible flow relations and look-up tables to determine properties within a supersonic flow field. The algorithm, developed for use in single species injection into air, allows for species data from injection of helium, nitrogen, ethylene, argon or air.

Both species sampling and conventional probing have associated measurement uncertainties. An error analysis is done by simple assumptions and traditional uncertainty propagation with 95% confidence intervals. The significant error sources in the Raman technique is systematic error in the optical calibration constants, and precision error from variations in individual measurements. Both these errors can be combined using the root of the sum of the squares (RSS) to give an uncertainty approximation of species number density. For this report, concentration data are nondimensionalized as equivalence ratio, Φ. The approximate uncertainty in equivalence ratio is 3.8%.

All flow property uncertainty obtained from conventional probing are computed by Fuller and reproduced here.[14] Error is approximated as follows: $\Delta P_t = \pm 2.8\%$, $\Delta M = \pm 1.7\%$, $\Delta \rho = 3.0\%$, $\Delta P = \pm 2.8\%$, $\Delta T = \pm 0.8\%$, $\Delta u = \pm 1.3\%$. These uncertainties are used to find the error in the derived quantities used in this report. Uncertainties in total pressure loss coefficient, $\bar{\omega}$, (defined later) is 4.3%.

F. Non-dimensionalization

Non-dimensionalization is performed on all presented data. Fluid properties are non-dimensionalized by their freestream values. All length quantities are divided by the diameter of the injection port. Similarly, all area values are non-dimensionalized by the injection port area.

It is important to characterize the injection characteristics in a fuel mixing study. Typically, this is done using the non-dimensional dynamic pressure ratio, $\bar{q}$ also known as the *jet-to-freestream momentum flux ratio*. This variable is defined by:

$$\bar{q} = \frac{\left(\rho u^2\right)_j}{\left(\rho u^2\right)_\infty} = \frac{\left(\gamma P M^2\right)_j}{\left(\gamma P M^2\right)_\infty} \qquad (3)$$

where subscript *j* indicates *jet properties at the injection port exit* and γ is defined as the *ratio of specific heats* and varies dependent upon flow conditions and species. Work by Schetz, et al presented a comprehensive survey of supersonic mixing of transverse and wall jets and found that many important mixing characteristics depend on $\bar{q}$.[15]

III.   Results

Data analysis can be separated into two categories: fuel mixing effectiveness and supersonic flow losses. This analysis is performed on each of the eight configurations at $x/d = 12$. Additional species concentration data are obtained for both the wide and baseline configurations at $x/d = 7.2$ and $x/d = 29.6$, allowing investigation into fuel mixing enhancement as the plume moves downstream. Data taken at $x/d = 12$ may be used as a comparison with previous research.[5]

Shadowgraphs are presented to orient the reader to overall flow field structure in the region of interest. Additionally, equivalence ratio end view contour plots obtained from Raman scattering measurements are shown and general comments on fuel plume shapes and concentration distributions are made.

A. Shadowgraph

Shadowgraphs allow for visualization of flow field structures. Of particular interest in supersonic flows are shock waves and expansion fans. It is important to note that shadowgraphs are two dimensional representations of highly three-dimensional flows, any interpretation of shock structures must be done carefully. For the present study, the shadowgraphs represent the flow field across a 6-inch span of the tunnel.

Figure 5 and Figure 6 show the shadowgraph images of the baseline and wide configurations, respectively, with injection for a $\bar{q}$ of 1.0 and 4.0 as indicated. The wide pylon configuration is representative of all pylon configurations and is the only shadowgraph shown below. Main flow in each image is from left to right, with the cavity positioned at the bottom of the images. The tunnel floor upstream of the cavity is visible as a light gray rectangular area on the bottom left of the figures. The cavity's backward facing step is also visible and begins at $x/d = 5.6$. The injection flow features of note are labeled in Figure 5a only but they appear in all configurations. Shock waves are visible in shadowgraphs as an alternation of light and dark bands of image intensity. Light shock waves formed from upstream disturbances are noticed crossing from the left of the images for all figures. Mach angles of the shock waves are approximately 28° corresponding to a flow Mach number of approximately 2.1. An expansion fan formed from the far upstream appears as a region of dark intensity between bands of lighter intensity. Once again, the origin of the axial direction ($x/d = 0.0$) is the injection port, and the origin of the transverse direction ($y/d = 0.0$) is the upstream lip of the cavity.

In each figure, the bow shock originates just upstream of the injection port and tends to be the strongest shock feature. In the baseline configurations, the bow shock initially penetrates perpendicular to the main flow due to the transverse fuel injection, then changes direction to match the main flow Mach angle. For the pylons, the bow shock's origin is displaced to the downstream tip of the pylon.   In all configurations, as $\bar{q}$ increases, the bow shock noticeably strengthens and displaces upward. An increase in barrel shock penetration can be seen as well. The important difference betweens the pylon and the baseline cases are the location of the bow shock origin, and the variation seen in apparent strength and initial shock angle.
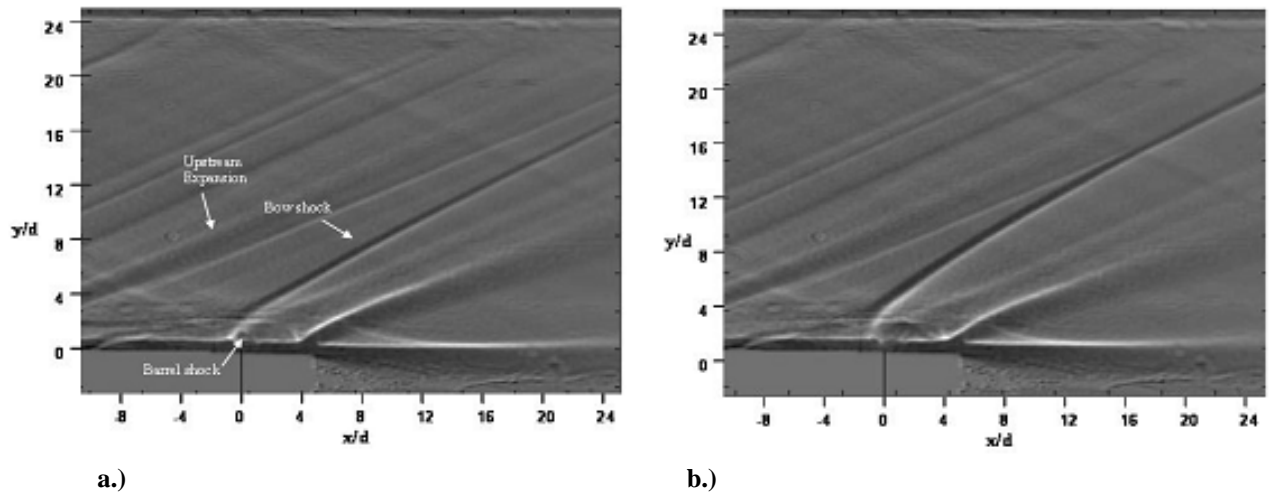

a.)   b.)

Figure 5. Shadowgraph of baseline configuration with $\bar{q}$ = a) 1.0 and b) 4.0
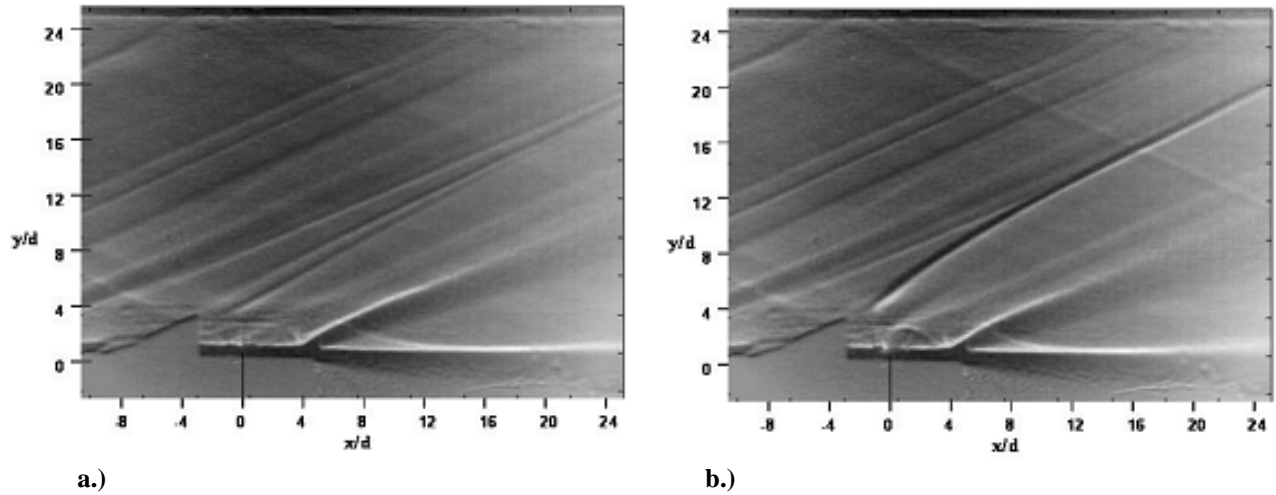
a.) **b.)**

Figure 6. Shadowgraph of wide pylon configuration with $\bar{q}$ = a) 1.0 and b) 4.0

## B. Species Composition Contour Plots

Figure 7 through Figure 10 show the time averaged contour profiles of ethylene equivalence ratio for each configuration at the measurement stations. The contours are oriented such that the reader is looking upstream toward the pylon. To aid in comparison between configurations, the contour color scales are the same for all plots. The minimum value of $\Phi = 0.1$ is used to ensure very low amounts of ethylene are tracked. The maximum value of $\Phi = 12.7$ corresponds to the maximum concentration found in the configurations. The fuel plumes' structures, sizes and locations within the test section are comparable to previous research indicating a good match in test conditions.[5]

Figure 7 gives the baseline's Φ contours at each of the three streamwise locations sampled with injection at $\bar{q}$ = 1.0 and 4.0 as indicated. At $x/d = 7.2$ (Figure 7a and Figure 7b), the fuel plume crowns and is at its most concentrated state. The counter-rotating vortices are clearly seen as two lobes for both $\bar{q}$ values. Most of the fuel is concentrated within the interior of the vortices and little mixing with the main flow is evident. The asymmetric way the ethylene concentrates within the left vortex at high $\bar{q}$ indicates the three-dimensionality of the flow. Plume penetration is reduced for the low $\bar{q}$ case due to the lower jet momentum. At $x/d = 12$ (Figure 7c and Figure 7d), the fuel plume begins to increase in area and fuel concentration within the vortices decreases. As axial distance increases, more fuel becomes entrained in the cavity ($y/d <= 0.0$). At $x/d = 29.6$, the plume is no longer dominated by the vortex structures. In the low $\bar{q}$ case, diffusion of fuel has clearly taken over and the presence of the vortex is no longer discernable; however, the maximum concentration of fuel (noted by maximum equivalence ratio, Φ_{max}) remains near the plume center. At the higher injection pressure, the counter-rotating vortices are still apparent, but have lost much of their previous resolution. The plume continues to expand in area and apparent penetration height. Overall, for both $\bar{q}$, Φ_{max} decreases as the plume moves downstream, a sign of fuel being transported away and air being transported into the interior of the plume where the fuel concentration is the highest.
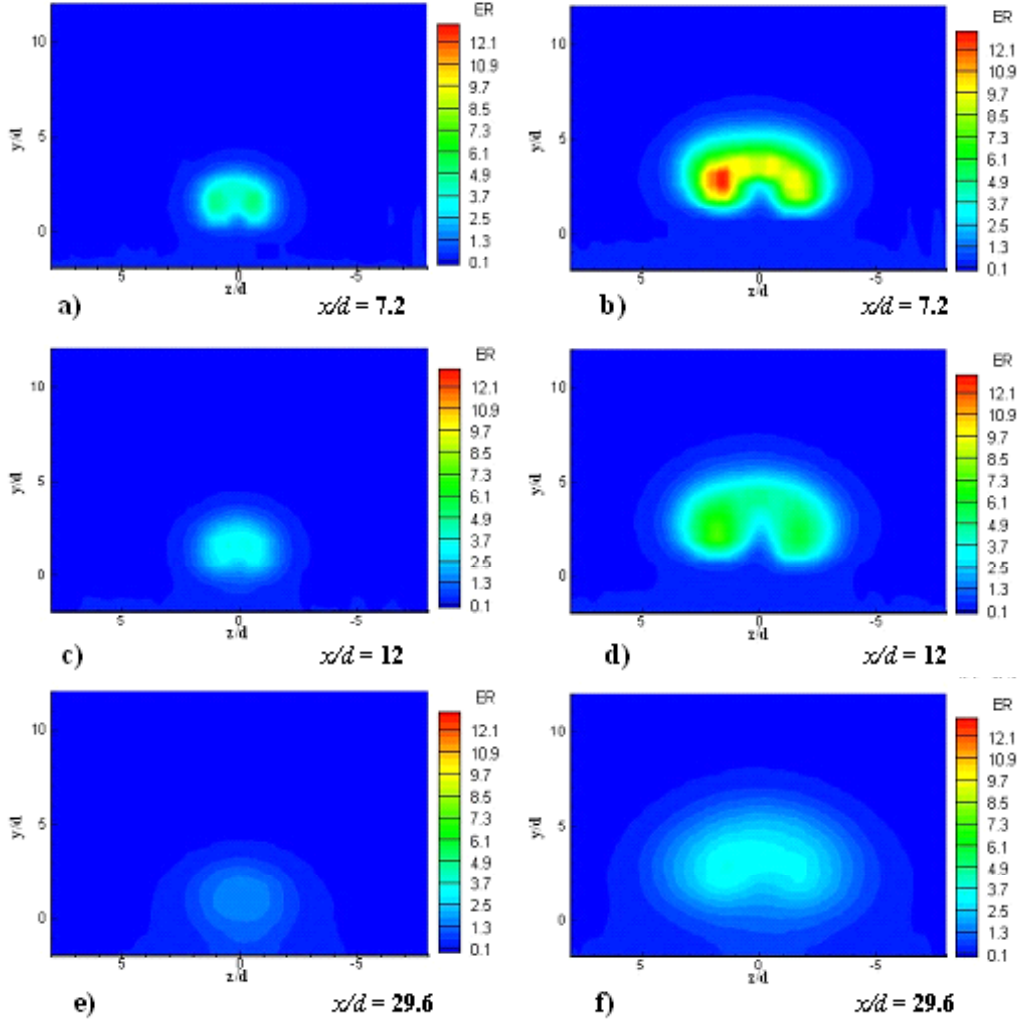
Figure 7. Baseline equivalence ratio contours for a), c), e) $\overline{q}$ = 1.0 and b), d), f) $\overline{q}$ = 4.0

Species concentration data are presented for the wide pylon at an x/d = 7.2, 12 and 29.6 in Figure 8. Results are presented in the same format as in the baseline configuration. At x/d = 7.2 it is apparent that the distribution of fuel is drastically changed due to the presence of the pylon. Penetration is increased and plume width is decreased compared with the baseline case. Additionally, Φ_{max} is lower for both $\overline{q}$ = 1.0 and 4.0. A third fuel lobe is present and the location of Φ_{max} is lifted above the vortex pair. Note that the asymmetric distribution of fuel in the vortex pair is opposite that seen in the baseline. This suggests an additional three-dimensional quality is added to the flow by the pylon shape and possible misalignment with the freestream. At x/d = 12 (Figure 8c and Figure 8d), the major concentration of fuel continues to migrate up away from the counter-rotating vortices into the freestream (for the high $\overline{q}$ case) and out away from the interior of the plume (for both high and low $\overline{q}$); little change is seen in the jet penetration for the lower injection pressure case. By x/d = 29.6 (Figure 8e and Figure 8f), the counter-rotating vortex pair seen in the high $\overline{q}$ case is almost totally absent as the plume continues to expand.
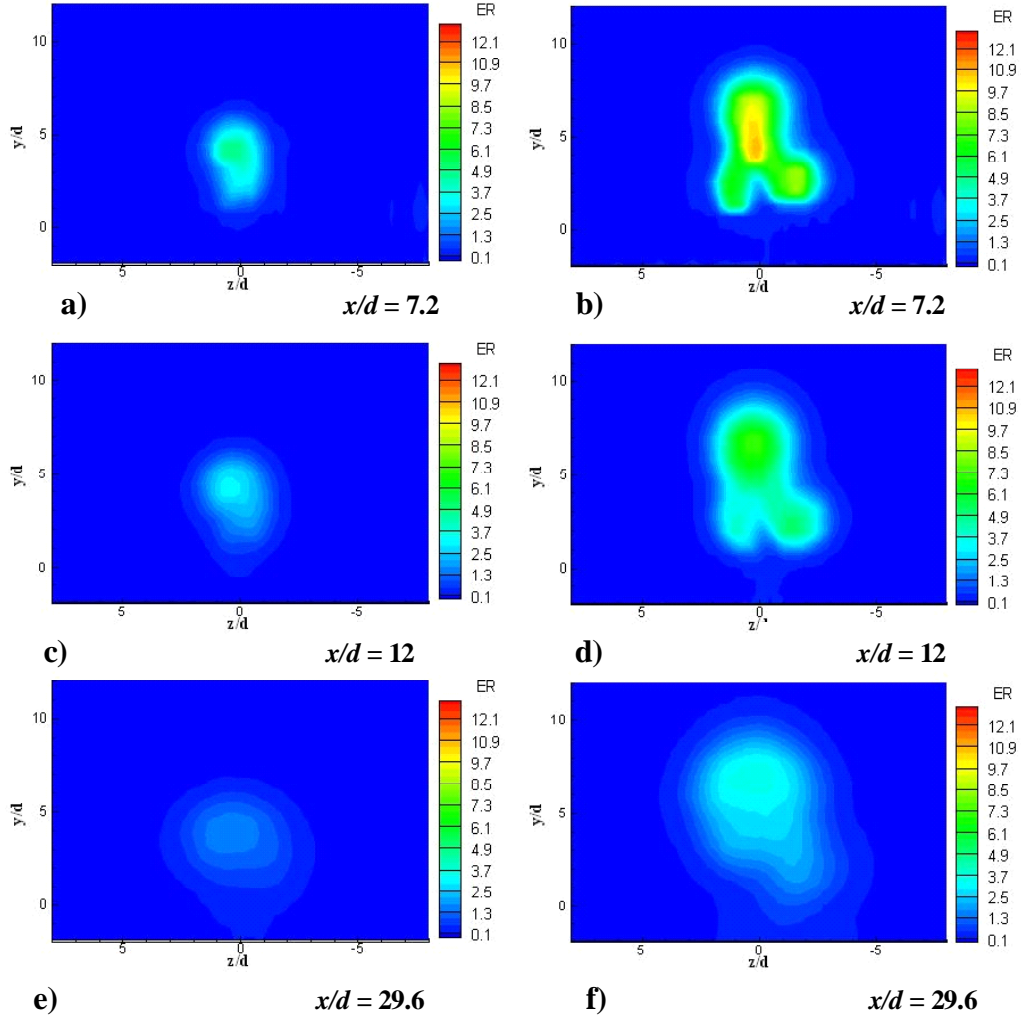
Figure 8. Wide pylon equivalence ratio contours for a), c), e) $\overline{q}$ = 1.0 and b), d), f) $\overline{q}$ = 4.0

Species concentration data are presented at a location of x/d = 12 for both the medium and tall configurations (Figure 9 and Figure 10 respectively). Comparison is made to both the baseline and wide configurations at the same axial location. The fuel plume structure and concentration distribution is similar in shape to the wide pylon. The two bottom lobes of fuel indicate the presence of the counter-rotating vortex pair. The location of Φ_{max} is again located above the counter-rotating vortices.
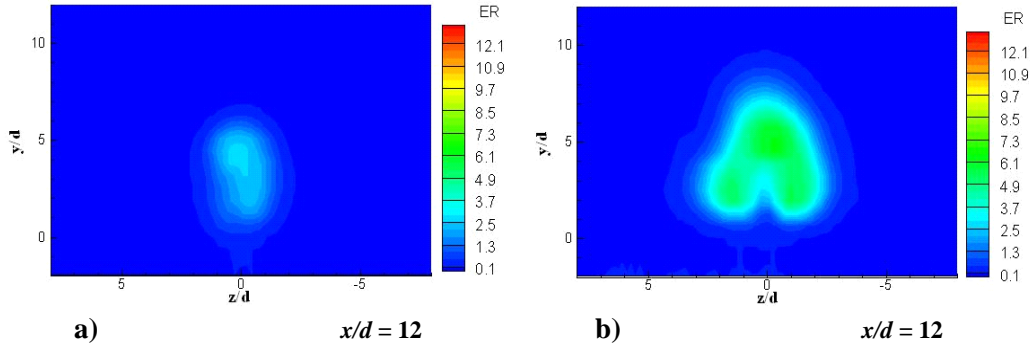
a)   *x/d* = 12   b)   *x/d* = 12

Figure 9. Medium pylon equivalence ratio contours for a) $\overline{q} = 1$ and b) $\overline{q} = 4$

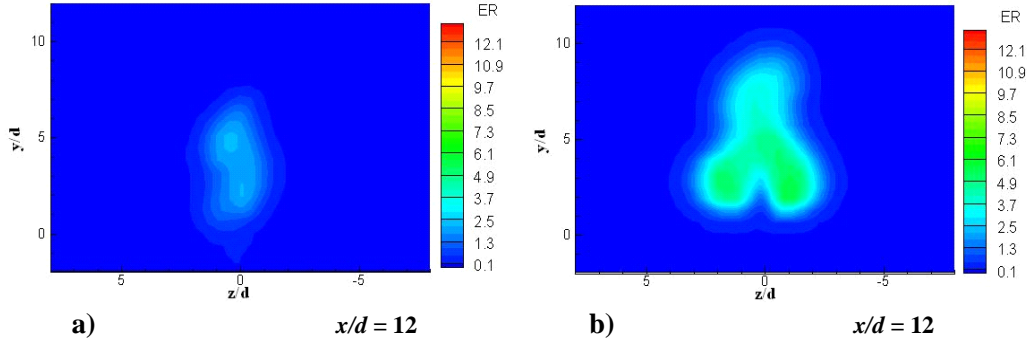a)   *x/d* = 12   b)   *x/d* = 12

Figure 10. Tall pylon equivalence ratio contours for a) $\overline{q} = 1$ and b) $\overline{q} = 4$

C. Mixing Analysis

Mixing analysis aims to investigate the ability to prepare fuel for quick and efficient burning over as large of a flow cross-section as possible. Examination of each configuration's mixing effectiveness is done primarily by analyzing the species concentration data.   All pylon configurations are compared against one another at *x/d* = 12. The availability of species concentration data at several axial locations (*x/d* = 7.2, 12 and 29.6) for the baseline and wide configurations allow for trajectory analyses and mixing rates to be obtained. Figures of merit for fuel mixedness in this study include: fuel plume penetration, maximum fuel equivalence ratio penetration, and plume area.

1. Fuel Penetration

Fuel plume penetration (h_p/d) is defined here as the maximum vertical height from the transverse centerline to the edge of the fuel plume, where Φ is 0.2. This value of the plume's edge is chosen because it is adequately below the ethylene-air lower flammability limit but high enough to define the fuel plume and separate it from fuel that becomes entrained within the cavity (which appears at Φ up to approximately 0.15).   The penetration of Φ_{max} (h_c/d) is also determined. The core of the fuel jet is assumed here to be at the location of Φ_{max}. This value is simply the vertical height above the transverse centerline to the location of the given configuration's value for Φ_{max}.
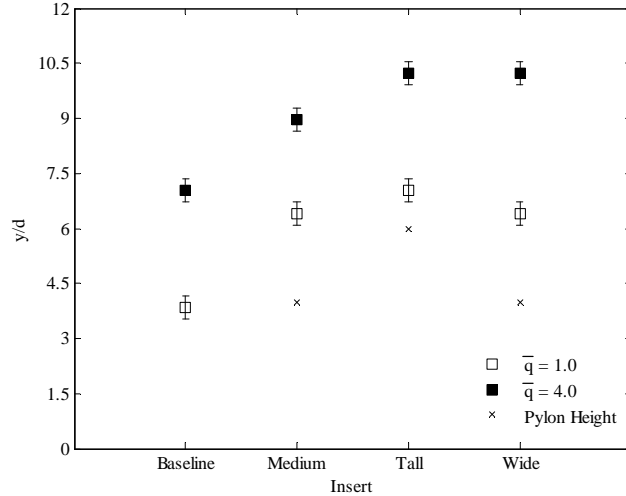
The plume penetration (h_p/d) is shown for each configuration in Figure 11. Pylon height is shown to compare plume penetration above each pylon. All fuel plumes penetrate higher than their respective pylon insert. As expected, the pylons increase plume penetration over that of the baseline for both values of $\overline{q}$. At $\overline{q}$ =1.0, the tall configuration's plume penetrates the highest over the baseline. As dynamic pressure ratio is increased to 4.0, plume penetration increases. At this injection condition, the wide and tall configurations have approximately the same plume penetration increase over the baseline, while the medium configuration has the least increase in plume penetration over the baseline. Of the three pylons, the wide sees a greater augmentation in plume penetration as $\overline{q}$ rises, while both the medium and tall pylons see approximately the same change.

As in the analysis of h_p/d, all configurations are compared at x/d of 12. Figure 12 presents the values of h_c/d for all configurations at both $\overline{q}$. Pylon height is again added to the figure. At low $\overline{q}$, all pylons see increase in h_c/d over the baseline case, with the tall pylon being the best performer. As $\overline{q}$ increases to 4.0, core penetration increases for all configurations. Both the medium and wide pylons see a positive change in core penetration as $\overline{q}$ is raised, with only the wide pylon's h_c/d increase being greater than that of the baseline. It is interesting to note that the tall configuration's h_c/d actually decreases and matches the baseline's value as injection pressure rises. This trend is seen in the tall pylon's Φ contour plots in Figure 10. The majority of the tall pylon's fuel concentration remains within the counter-rotating vortices.

Overall, at x/d = 12, both h_p/d and h_c/d for each pylon configuration show increases in penetration over the baseline for both injection pressures. At $\overline{q}$ =1.0, h_p/d and h_c/d scale proportionally to pylon height. However, this is not the case in the $\overline{q}$ = 4.0 case. Both the wide and medium pylons sustain the core of the fuel plume above the counter-rotating vortices; this allows maximum penetration of the plume into the freestream. The tall pylon's inability to sustain the core of the plume above the vortex pair at high $\overline{q}$ hinders its ability to improve penetration over the baseline effectively. This issue may be due to pylon aspect ratio. The wide pylon shows the best plume and core penetration improvement over the baseline.

Figure 11. Plume penetration (h_p/d) comparison between inserts at x/d = 12
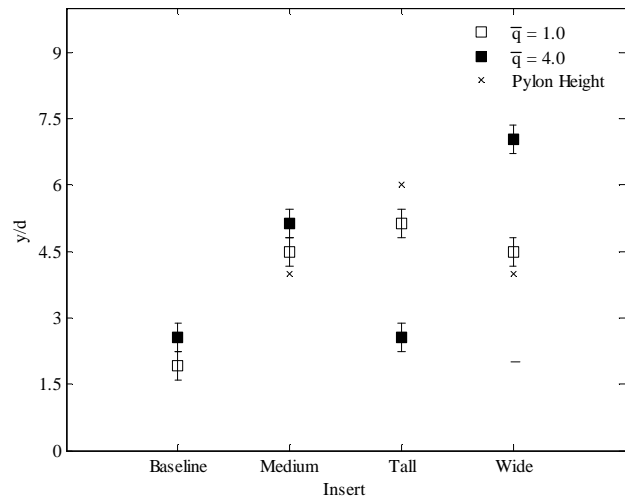
Figure 12. Plume core penetration (h_c/d) comparison between inserts at x/d = 12

2. Decay of Maximum Equivalence Ratio

The plume and core penetration trajectories for the wide and baseline configurations are evaluated at both injection pressures. Plume penetration trajectory is defined as the variation in plume penetration with downstream

distance. The downstream locations used to determine the penetration trajectories are x/d = 7.2, 12 and 29.6. The values of Φ_{max} for each configuration give an idea of the distribution of fuel within the plume. Since the same amount of mass is injected for a given value of $\bar{q}$ regardless of injector configuration, a smaller value of Φ_{max} indicates better fuel-air mixing than a larger value. It is also expected that for an increase in downstream distance from the injection source, the fuel plume deteriorates and becomes increasingly mixed with the surrounding air. Past studies show that plume data varies exponentially in the far-field region.[15] Therefore, power-law curve fits are used to predict the rate of change in decay with downstream location. The power law used is of the following form:
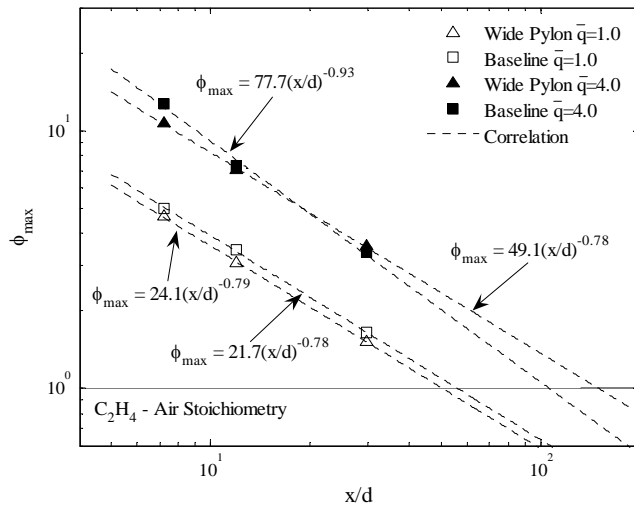
$$\phi_{\max} = \beta \left(\frac{x}{d} \right)^{n} \qquad (4)$$

Where the values for β and n are found using the method of least squares. The exponent n relates the rate of change of the variable of interest. A larger overall rate of decay is desirable and is indicated by a larger, negative value for n. The average rate of decay of -0.8 for jets in a crossflow[15] compares well with the rates in this report.

Figure 13 shows the decay of maximum equivalence ratio with downstream distance for the wide and baseline configurations. The data are presented with a logarithmic scale on both the vertical and horizontal axes. Error bars are not shown due to their small relative size. At $\bar{q}$ = 1.0, there is no significant difference in the decay rate of the wide and baseline configurations, both values of n are at approximately -0.78. When $\bar{q}$ increases to 4.0, the rate of decay for the wide pylon stays about the same, while the rate for baseline increases to about -0.93. Note that for the high $\bar{q}$ case, a transition between the wide's faster near-field mixing and the baseline's faster far-field mixing occurs at $x/d \approx 20$. This is due to the wide pylon's initially lower fuel concentration and the baseline's greater rate of concentration decay.

Typically, once the maximum concentration of a fuel reaches stoichiometric conditions, the injectant is considered fully mixed[15]; the entire fuel plume is at or below

Figure 13. Maximum equivalence ratio decay vs. axial distance for wide and baseline inserts

the composition needed for total combustion. For this reason, a straight line at stoichiometric Φ is drawn on the figure. The fully mixed distance, x_{fm}, is desired to be small and is a factor of both rate of concentration decay and initial magnitude of Φ. For low $\bar{q}$, x_{fm} is approximately $50d$ and $60d$ for the wide pylon and baseline respectively. At the high $\bar{q}$ condition, x_{fm} increases to about $150d$ and $110d$ for the wide pylon and baseline respectively. These values for high injection pressure are at the same order of magnitude as the historical x_{fm} trend of approximately $200d$.[15]

The accepted practice of determining a flow to be fully mixed once the maximum concentration of fuel reaches stoichiometric is perhaps not the best gauge of a specific fuel's mixing for combustibility (although it does give a fixed point of comparison to previous research done with varying fuel types). Typically, most hydrocarbon fuels burn at concentrations above stoichiometric. It may be prudent to establish how far downstream it takes for a plume's maximum concentration to reach the upper flammability limit (Φ_U) for a specific fuel. The published value of Φ_U for an ethylene-air mixture at standard temperature and pressure is 5.5.[16] The distance required for an ethylene plume's maximum concentration to reach Φ_U, is termed in this report as the flammable mixture distance x_{flam}. In other words, at x_{flam}, the entire plume is at or below the concentration of fuel required for combustion. At $\bar{q}$ = 1.0, the values of x_{flam} for the wide and baseline configurations are about $1d$ and $2d$ respectively, almost immediately after injection. This low value for x_{flam} is due to the low amount of mass being injected into the

freestream. At $\bar{q}$ = 4.0, the value of x_{flam} for each the wide and baseline configurations is almost identical at approximately 20d.
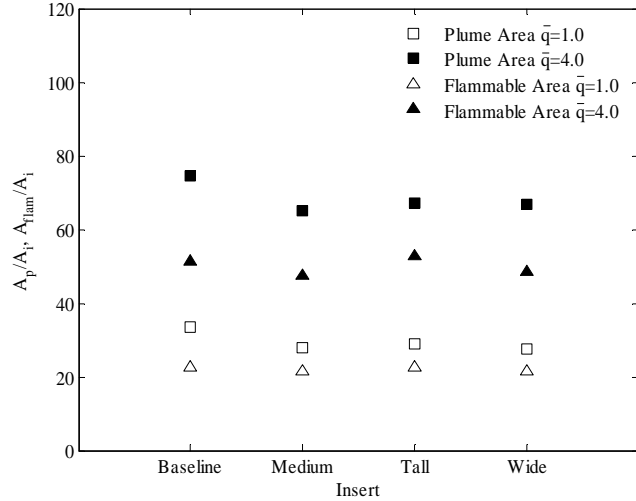
3. Plume Area

Total plume area (A_p) is determined from the definition of the plume edge, where the plume is the area encompassing the outermost contour at Φ = 0.2. Another useful area used in this report is the flammable plume area (A_f), where A_f is defined as the area of the plume that has fuel concentration between the published upper and lower flammability limits of ethylene in air at standard temperature and pressure (Φ_U = 5.5 and Φ_L = 0.4 respectively, but a 10% buffer is added to narrow the limits used in the research to 5.0 and 0.36 to account for variation).[16] This figure of merit represents the area of the fuel plume that is in the proper concentration for combustion. Comparisons are made for both A_f and Ap in all configurations at an x/d of 12. Plume spreading is determined for the wide and baseline inserts as the change in both A_f and Ap with downstream distance. As performed in previous sections, the trajectory analysis uses measurements at x/d of 7.2, 12 and 29.6. As before, all data are determined at both $\bar{q}$ = 1.0 and 4.0. Error bars are not shown due to their small relative size.
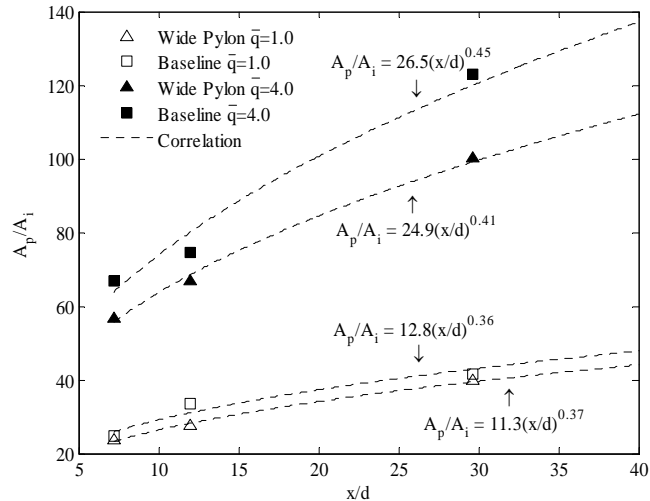

Figure 14. Total (A_P) and flammable plume (A_f) area comparison for all inserts at x/d = 12

Figure 14 shows the total and flammable plume areas (A_p and A_f) normalized by the injection port area A_i for all test cases at x/d = 12. All pylons demonstrate approximately the same total and flammable area when compared at the same injection pressure. An increase in injection pressure causes an increase in both total and flammable plume areas. The baseline configuration shows a noticeably larger A_p compared to the pylons. However, when comparing A_f, the difference between the baseline and the pylon configurations is not as significant since more of the baseline plume is not within the flammability limits than the other configurations. Both the baseline and tall configurations appear to have slightly larger flammable plume areas than the wide and medium pylons, however, this increase is not substantial enough to deem either the baseline or tall configurations as superior at this streamwise station.

Figure 15. Total plume area (A_p) trajectory for baseline and wide inserts

4. Plume Spreading

As axial distance from the injection port increases, the plume is expected to dissipate and enlarge. This causes increases in both A_p and A_f. This section compares spreading of A_p and A_f with downstream distance for both the baseline and wide inserts. Figure 15 and
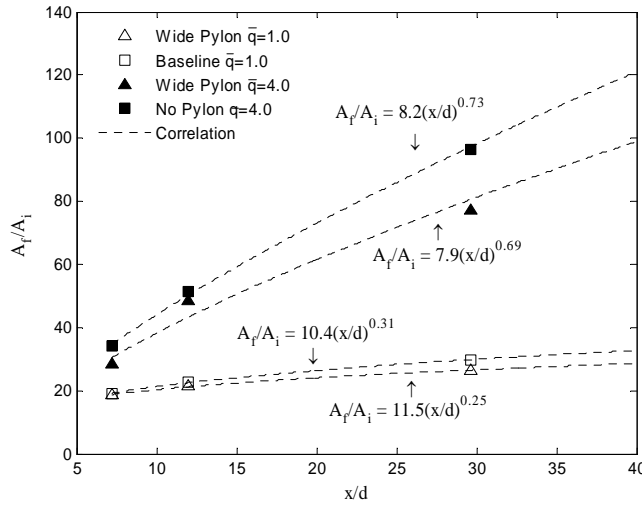
14

Figure 16. Flammable plume area (A_f) trajectory for baseline and wide inserts

Figure 16 show the total plume area (A_p) and flammable plume area (A_f) spreading respectively for the two configurations taken at axial locations of x/d = 7.2, 12 and 29.6. As in previous trajectory plots, a power law correlation of the form seen in Equation 4 is added to each case. Plume spreading trajectories for A_p given in Figure 15 show that for both injection pressures, the baseline configuration has increased spreading compared to the wide pylon over the region tested. At low $\overline{q}$, baseline A_p has a greater magnitude, but similar spreading rates to the wide. When $\overline{q}$ is increased to 4.0, both the magnitude and spreading rates are increased in both configurations. At the higher injection pressure, the baseline shows better overall magnitude and spreading rate compared to the wide. Trajectories of A_f shown in Figure 16 display similar trends to those seen for A_p. At both injection pressures, the baseline cases demonstrate larger magnitudes of A_f at each axial location and spreading rates compared to the wide. With increasing injection pressure, a positive change in both A_f and n is noticeable. It is also interesting to note that for both low $\overline{q}$ configurations, rate of spreading of A_f is less than the rate of spreading of A_p. This suggests that most of the plume is spreading in concentrations outside of the flammability limits. The opposite is seen in the high $\overline{q}$ cases; the rates of flammable plume spreading are greater than the rates of total plume spreading, indicating that the plume's fuel is mixing into concentrations within the upper flammable limit faster than in the total plume is spreading.

Overall, the baseline configuration at both injection pressures displays better total and flammable plume spreading than the wide pylon configuration. This may be due in part to the baseline cases' fuel plume being located within the vortex pair, which aids in mixing and spreading. As injection pressure increases, the magnitude and rate of spreading of A_p and A_f increases, indicating that increasing $\overline{q}$ has a favorable effect on plume spreading. Additionally, at high $\overline{q}$, A_f's rate of spreading is greater than that of A_p for both configurations. At low $\overline{q}$, A_f's rate of spreading is less than that of A_p. This may be seen when examining the equivalence ratio contours in Figure 7 and Figure 8. As axial distance increases the fuel within the plume disperses. For low $\overline{q}$ (lower mass injected), at x/d = 7.2, the maximum equivalence ratio within the plumes starts below Φ_U. Therefore, as the plume fuel dissipates and mixes, fuel concentration drops below Φ_L without any new fuel added. For the high $\overline{q}$ cases at the same axial location, the maximum equivalence ratio starts above Φ_U, so as fuel dissipates below Φ_L, fuel at high concentrations is also mixing into flammable limits at a higher rate. Eventually, the maximum equivalence ratio for high $\overline{q}$ cases will eventually drop below Φ_U. Once this occurs, both injection pressures' area spreading rates may be similar.

D. Aerodynamic Loss Analysis

Quantifying aerodynamic losses is defined within as total pressure loss. Total pressure losses are determined from total pressure contours and a total pressure loss coefficient. The following sections discuss and compare total pressure for each configuration at x/d = 12.
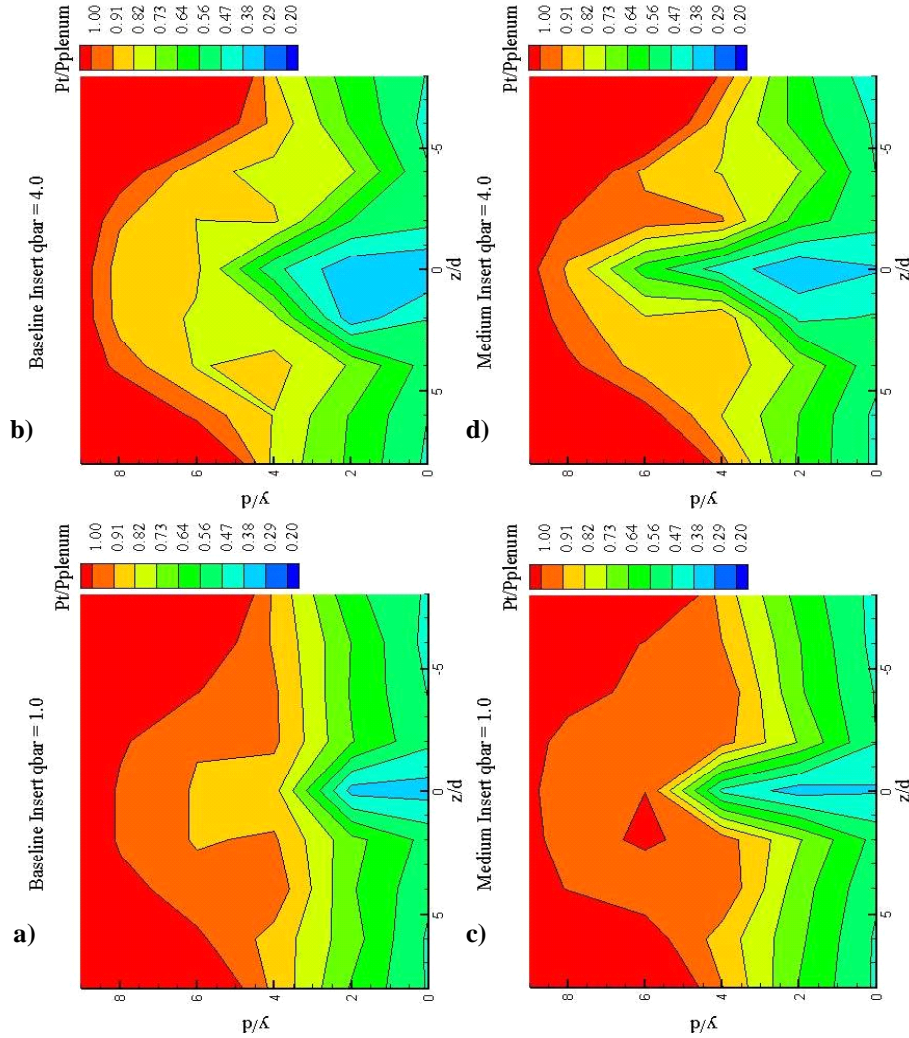
1. Total Pressure Contours

Figure 16 and Figure 17 give the normalized P_t contours at an axial location of x/d = 12 for all eight conditions tested. Normalization is done against the tunnel plenum pressure, which represents the total pressure upstream of the combustor section. The axes are aligned in the same manner seen in the species concentration contours. The spatial range varies from -8 ≤ z/d ≤ 8 and 0 ≤ y/d ≤ 9. Contour color bars are scaled consistently to aid in plot-to-

plot comparisons. The bow shock is seen as a curved contour under which the values for normalized total pressure are less than 1.0. For this analysis, the region of interest is the area beneath the shock.

The baseline $\overline{q}$ = 1.0 and 4.0 cases are shown in Figure 16 a) and b) respectively. The location of the fuel plume is evident by the region of low pressure penetrating into the freestream. The surrounding low total pressure region is due to the counter-rotating vortices transferring kinetic energy into the transverse direction. Because of the low resolution, the vortex structures are unidentifiable, but their overall effect of lowering total pressure can be clearly seen. The region of low total pressure near the bottom of the figure is due to diffusion of the lower momentum fluid from the cavity and the wake behind injection. Notice in the high $\overline{q}$ case, the asymmetric quality of the jet plume is evident, and increased total pressure loss occurs in the left lobe (left side of centerline) where a higher fuel concentration is present. Also apparent in the high $\overline{q}$ case, total pressure losses penetrate further into the flow. Overall, greater pressure recovery is evident in the low $\overline{q}$ case.

The medium pylon is seen in Figure 16 c) and d). Similar physical features are apparent in the medium configurations as seen in the baseline. Higher fuel plume penetration brings total pressure loss upward into the flow, but the gradients are less severe since the losses are distributed further. Again, as injection pressure increases, the plume losses encompass a greater area and there is less total pressure recovery.

Figure 16. Normalized baseline and medium total pressure contours at x/d = 12
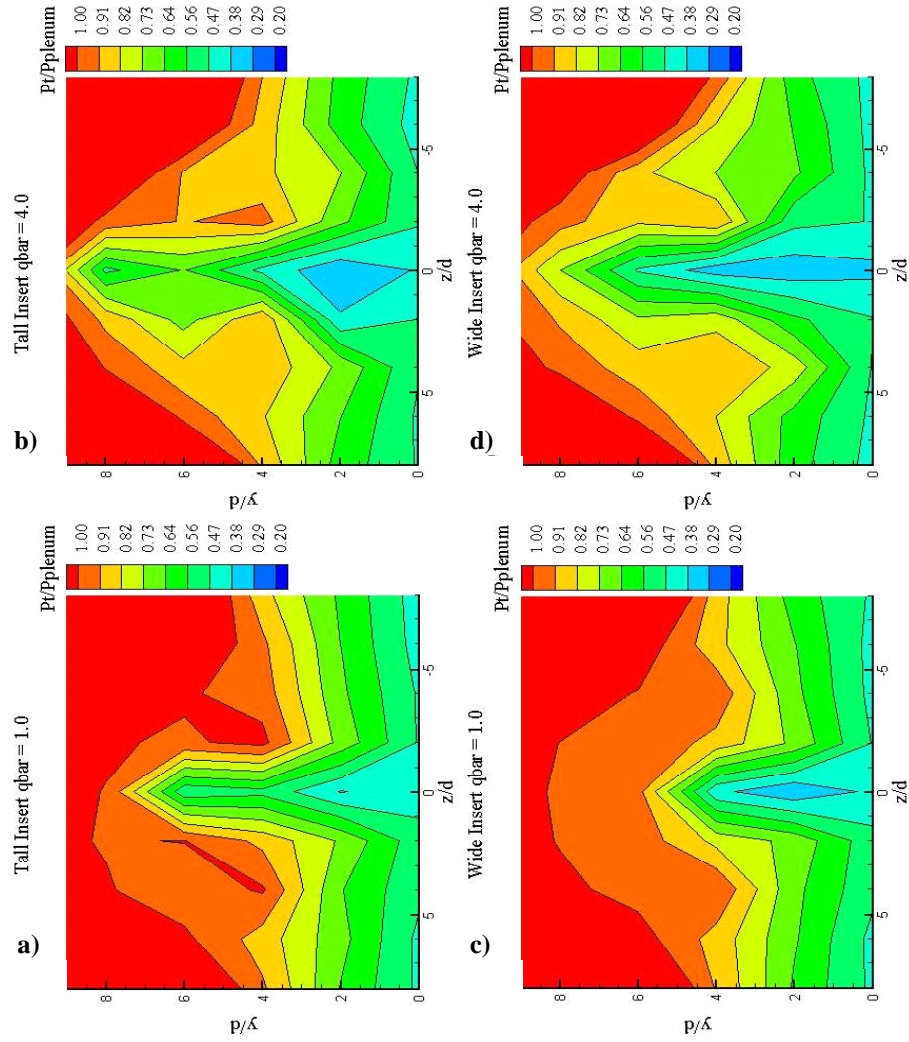
Figure 17. Normalized tall and wide total pressure contours at *x/d* = 12

The tall pylon's P_t contours, are shown in Figure 17 a) and b). The increased height of the pylon causes the flow losses to penetrate farther into the core flow than the medium pylon, but seems to distribute P_t losses better than the medium. As injection pressure increases, bow shock strengthens, and losses penetrate further into the flow. However the losses are unevenly distributed, with the majority of the losses being concentrated near the bottom of the pylon. This occurrence is most likely due to the lower location of the fuel plume core within the counter-rotating vortices. The total pressure losses for the wide pylon, shown in Figure 17 c) and d), are very similar to those seen in the medium pylon, due to their similar geometry. It appears that the added width of the wide pylon slightly widens the total pressure loss distribution.

By visual observation of Figure 16 and Figure 17, the pylons do not appear to greatly alter the total pressure recovery compared with the baseline in the area below the bow shock. The pylons do appear to distribute the losses into the flow more effectively than the baseline due to their increased plume penetration.
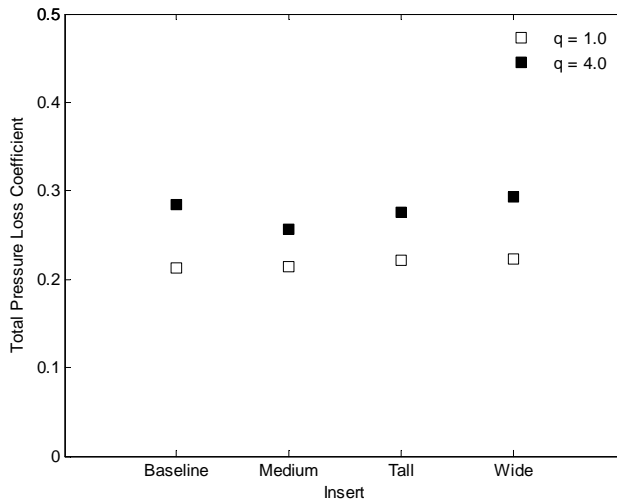
2. Pressure Loss Coefficient

The total pressure loss coefficient, defined as $\bar{\omega}$ provides a mass-averaged fraction of total pressure loss for a given field and is represented in the equation below.

$$\bar{\omega} = 1 - \frac{\bar{P}_t}{P_{t_{ref}}} \qquad (5)$$

Where $\bar{P}_t$ is the *mass-averaged total pressure* for a region of interest and $P_{t_{ref}}$ is the *measured tunnel plenum pressure*. Values for $\bar{P}_t$ may be found using the equation below.

$$\bar{P}_t = \frac{\int P_t \rho u dA}{\int \rho u dA} \qquad (6)$$

This definition allows for the local impact of flow momentum through an area. An $\bar{\omega} = 1$ means complete P_t loss and $\bar{\omega} = 0$ denotes no P_t loss. Therefore, a small value for $\bar{\omega}$ is desired. Mass averaging is performed across a cross section consistent for all configurations. The cross section spans from $-8 \leq z/d \leq 8$ and varies in the transverse coordinate to avoid the effect of the bow shock and ensure capture of the plume. At the edges of the cross section, the transverse coordinate varies from $0 \leq y/d \leq 6$ and $0 \leq y/d \leq 6$ at the centerline. Figure 18 gives values of $\bar{\omega}$ for each configuration at $x/d = 12$. In the low injection pressure cases, $\bar{\omega}$ remains fairly consistent. All pylons have slightly increased total pressure loss compared with the baseline at $\bar{q} = 1.0$. The most sizeable increase at this injection pressure occurs in the tall and wide configurations, as the pylons have larger cross-sectional areas compared to the medium and baseline inserts. As $\bar{q}$ increases to 4.0, the pressure losses increase. This is to be expected when viewing both the shadowgraphs and total pressure contour plots. The increased plume area and momentum strengthens the bow shock and introduces larger regions of total pressure reduction into the flow. Most pylon's $\bar{\omega}$ are actually reduced compared to baseline. Again taking into account uncertainty, the tall and wide pylons show little change compared with the baseline, only the medium pylon shows sizeable decrease in pressure loss compared with baseline. Overall, all results are similar with respect to total pressure losses for a given injection pressure.

Figure 18. Total Pressure Loss Coefficient

IV.   Conclusion

Three pylon-based fuel injectors were experimentally investigated and compared against a simple baseline injection case. All injectors issued into a Mach 2 crossflow to stimulate the environment inside a scramjet combustor section. In each case, two injection pressures were studied. Measurements of mixing and flow losses were of primary interest. Mixing was characterized by fuel penetration, maximum plume equivalence ratio, and plume area. Furthermore, qualitative treatment of equivalence ratio contour plots allowed general observations into the mixing qualities produced by each configuration. Losses were parameterized by the total pressure loss coefficient. Total pressure contours allowed observations of losses seen in the flow field. Data for all

configurations were obtained taken at $x/d = 12$, additional species sampling data were obtained at $x/d = 7.2$ and 29.6 for the wide pylon and baseline configurations.

All pylon configurations demonstrated better penetration and shifted the fuel plume core higher into the crossflow compared with the baseline at both $\bar{q}$. The pylons lifted the fuel plumes higher above the cavity allowing better fuel dispersion into the main flow. While pylons demonstrated slightly lower values of maximum equivalence ratio, similar mixing effectiveness to the baseline was noticed. Pylon presence contributed to increased spreading, but their weaker counter-rotating vortices had less of an impact on mixing when compared with the baseline. Mixing in the vortex pair was reduced because the core of the pylons' fuel plume was lifted out of the vortices. The strength of the vortex pair was dictated by the amount of fuel entrained within. Pylon presence did not contribute to greater aerodynamic losses than the baseline; in fact, losses attributed to the pylons were similar to if not slightly lower than those found in the baseline. Increase in form drag introduced by the pylons was offset by the highly oblique bow shock produced. Injection pressure held the strongest influence on both mixing and loss.

Due to its size and geometric shape the medium pylon proved to be a nominal performer in all aspects. It provided the lowest overall increase in penetration of all pylons, and displayed smaller (if similar) plume area sizes than the other pylons. It indicated similar total pressure and momentum losses when compared to the baseline, and no significant improvement was noticed.

The tall pylon demonstrated interesting mixing and loss traits. It provided the highest plume penetration at the low $\bar{q}$ but its fuel plume core location within the counter-rotating vortices prevented a sizeable increase in penetration at the high $\bar{q}$ case. However, this location of the plume core aided mixing better than the other pylons. The larger size of the tall pylon did not appear to contribute significantly to drag.

The wide pylon provided the best overall mixing performance of all the pylons. While similar to the tall and medium, it did provide slightly better values for penetration (at high $\bar{q}$), plume area and flammability. Losses appeared to be minimized in the wide configuration, and it provided the lowest values for the total pressure loss coefficient, indicating comparable to slightly better flow losses to the baseline. Additionally, the wide pylon's trajectory characteristics were similar to the baseline despite the location of the wide's fuel plume outside the counter-rotating vortices.

Acknowledgments

The views expressed in this article are those of the author and do not reflect the official policy or position of the United States Air Force, Department of Defense, or the U.S. Government.

References

[1] Gruber, M. R., Baurle, R. A., Mathur, T., Hsu, K.-Y., "Fundamental Studies of Cavity-Based Flame holder Concepts for Supersonic Combustors," AIAA Paper 99-2248, June 1999.

[2] Mathur, T., Gruber, M. R., Jackson, K., Donbar, J., Donaldson, W., Jackson, T., Billig, F., "Supersonic Combustion Experiments with a Cavity-Based Fuel Injector", *Journal of Propulsion and Power*, Vol. 17, No. 6, 2001, pp. 1305-1312.

[3] Livingston, T., Segal, C., Schindler, M., Vinogradov, V. A., "Penetration and Spreading of Liquid Jets in an External-Internal Compression Inlet", *AIAA Journal*, Vol. 38, No. 6, 2000, pp. 989-994.

[4] Vinogradov, V. A., Owens, M., Mullagiri, S., Segal, C., "Effects of Fuel Pre-Injection on Mixing in a Mach 1.6 Airflow," AIAA Paper, 99-45503, November 1999.

[5] Montes, D.R., "Mixing Effects of Pylon-Aided Fuel Injection Located Upstream of a Flameholding Cavity in Supersonic Flow," AFIT Thesis AFIT/GAE/ENY/05-M12, (Mar 05).

[6] Gouskov, O., Kopchenov, V., Vinogradov, V., "Numerical Research of Gaseous Fuel Pre-injection in Hypersonic 3-D Inlet," AIAA Paper, 2000-3599, July 2000.

[7] Livingston, T., Segal, C., "Penetration and Spreading of Liquid Jets in an External-Internal Compression Inlet," *AIAA Journal*, Vol. 38, No. 6, 2000, pp. 989-994.

[8] Owens, M. G., Mullagiri, S., Segal, C., "Effects of Fuel Preinjection on Mixing in Mach 1.6 Airflow," *Journal of Propulsion and Power*, Vol. 17, No. 3, 2001, pp. 605-610.

[9] Gruber, M. R., Nejad, A. S., "New Supersonic Combustion Research Facility," *Journal of Propulsion and Power*, Vol. 11, No. 5, 1995, pp. 1080-1083.

[10] Anderson, John D. Fundamentals of Aerodynamics. 3rd Ed. New York: McGraw-Hill. 2001.

[11] Demtröder, Wolfgang. Laser Spectroscopy: Basic Concepts and Instrumentation. New York: Springer-Verlag. 1981.

[12] Eckbreth, Alan C. Laser Diagnostics for Combustion Temperature and Species. Cambridge: Abacus. 1988.

[13] Fuller, Raymond P., "Fuel-Vortex Interactions for Enhanced Mixing In Supersonic Flow," Ph.D. Dissertation, Department of Aerospace and Ocean Engineering, Virginia Polytechnic Institute and State University, Blacksburg, VA, 1996.

[14] Fuller, R. P., Wu, P., Nejad, A. S., Schetz, J. A., "Comparison of Physical and Aerodynamic Ramps as Fuel Injectors in Supersonic Flows," *Journal of Propulsion and Power*, Vol. 14, No. 2, 1998, pp. 135-145.

[15] Schetz, J. A., Thomas, R.H., and Billig, F. S. "Mixing of Transverse Jets and Wall Jets in Supersonic Flow," *Seperated Flows and Jets,* edited by V.V. Kozlov and A.V. Dovgal, Springer-Verlag, Berlin, 1991.

[16] Glassman, Irvin. Combustion. 3rd ed. New York: Academic Press, 1996.